

Draft: October 30, 2018

A Dual Narrowband Survey for $H\alpha$ Emitters at $z=2.2$: Demonstration of the Technique and Constraints on the $H\alpha$ Luminosity Function¹

Janice C. Lee^{1,2,10,12}, Chun Ly^{2,11}, Lee Spitler⁴, Ivo Labbé^{5,1}, Samir Salim⁶,
S. Eric Persson¹, Masami Ouchi^{7,8,1}, Daniel A. Dale⁹, Andy Monson¹, David Murphy¹

ABSTRACT

We present first results from a narrowband imaging program for intermediate redshift emission-line galaxies using the newly commissioned FourStar infrared camera at the 6.5m Magellan telescope. To enable prompt identification of $H\alpha$ emitters, a pair of custom 1% filters, which sample low-airglow atmospheric windows at 1.19 μm and 2.10 μm , is used to detect both $H\alpha$ and $[\text{OII}]\lambda 3727$ emission from the same redshift volume at $z=2.2$. Initial observations are taken over a 130 arcmin² area in the CANDELS-COSMOS field. The exquisite image quality resulting from the combination of the instrument, telescope, and standard site conditions ($\sim 0''.55$ FWHM) allows the 1.19 μm and 2.10 μm data to probe 3σ

¹Carnegie Observatories, 813 Santa Barbara Street, Pasadena, CA

²Current address: Space Telescope Science Institute, Baltimore, MD

³Visiting Astronomer, SSC/IPAC, Caltech, Pasadena, CA

⁴Centre for Astrophysics and Supercomputing, Swinburne University of Technology, Australia

⁵Leiden Observatory, Leiden University, Leiden, The Netherlands

⁶Astronomy Department, Indiana University, Bloomington, IN

⁷Institute for the Physics and Mathematics of the Universe (IPMU), TODIAS, The University of Tokyo, Japan

⁸Institute for Cosmic Ray Research, The University of Tokyo, Japan

⁹Department of Physics and Astronomy, University of Wyoming, Laramie, WY

¹⁰Carnegie Fellow

¹¹Giacconi Fellow

¹²jlee@stsci.edu

emission-line depths down to 1.0×10^{-17} erg s $^{-1}$ cm $^{-2}$ and 1.2×10^{-17} erg s $^{-1}$ cm $^{-2}$ respectively, in less than 10 hours of integration time in each narrowband. For H α at $z = 0.8$ and $z = 2.2$, these fluxes correspond to observed star formation rates of ~ 0.3 and ~ 4 M $_{\odot}$ yr $^{-1}$, respectively. We find 122 sources with a 1.19 μ m excess, and 136 with a 2.10 μ m excess, 41 of which show an excess in both bands. The dual narrowband technique, as implemented here, is estimated to identify $\gtrsim 80\%$ of $z = 2.2$ H α emitters in the narrowband excess population. With the most secure such sample obtained to-date, we compute constraints on the faint-end slope of the $z = 2.2$ H α luminosity function. Fitting of a pure power-law gives $\alpha = -1.85 \pm 0.31$, which is steeper than other recent estimates based on coarser selection techniques, but consistent within the typically large uncertainties that currently characterize such measurements. Combining our LF points with those at higher luminosities from other work, the slope decreases to $\alpha = -1.58 \pm 0.40$. These “narrow-deep” FourStar observations have been obtained as part of the larger NewH α Survey, which will combine the data with “wide-shallow” imaging through a similar narrowband filter pair with NEWFIRM at the KPNO/CTIO 4m telescopes, to enable study of both luminous (but rare) and faint emission-line galaxies in the intermediate redshift universe.

Subject headings: galaxies: evolution — galaxies: photometry — infrared: galaxies — surveys — techniques: photometric — galaxies: star formation

1. Introduction

The rest-frame optical emission lines are indispensable diagnostics of the activity in galaxies. In the local Universe, the measurement of lines from [OII] $\lambda 3727$ through [SII] $\lambda \lambda 6716, 31$ has traditionally provided essential information on properties such as the star formation rate (SFR); the physical state of the ISM (e.g., electron temperatures and densities, gas-phase metallicities); the dust reddening; and may also indicate whether an AGN is present. Thus, it may seem like a conspiracy of nature that for $1 < z < 3$, where star formation and AGN activity reach their global maxima (Shapley 2011 and references therein) and observing these lines is critical to the study of galaxy evolution, they are shifted into the near-infrared, where spectroscopic observations from the ground are difficult due to the bright sky background.

¹This paper is primarily based upon data gathered with the 6.5 meter Magellan Telescopes located at Las Campanas Observatory, Chile.

One way to partially circumvent the difficulties posed by the forest of near-infrared terrestrial lines is to use narrowband filters which are designed to transmit in dark regions of the sky spectrum. Such filters can be employed to blindly detect and measure emission lines at select redshifts. In the past, this technique has been successfully used with red-sensitive optical imagers to search for Ly α emitters at the highest redshifts (e.g., Taniguchi et al. 2003 and references therein). However, the near-IR instrumentation required to enable analogous surveys for galaxies via their rest-frame optical emission lines at “cosmic high noon” became readily available only around the mid-2000’s. Initial attempts with the first generation of IR imagers with small fields-of-view were heroic, but had limited success. For example, Teplitz et al. (1998) collected a total of ~ 48 hours of Keck observations with NIRC (38'' FoV), and found a sample of just 13 candidates. Even up to 2007, only a couple of hundred measurements of H α in field galaxies past $z \sim 0.4$ had been published (e.g., Tresse et al. 2002; Erb et al. 2006c). With the gradual maturation of wide-field near-infrared cameras however, efforts by a few independent groups (Villar et al. 2008; Geach et al. 2008; Sobral et al. 2009; Hayes et al. 2010), including our own (Ly et al. 2011; J.C. Lee et al. 2012, in preparation), have now succeeded in increasing the total number of candidate H α emitters at $z > 0.8$ by an order of magnitude.

Nevertheless, while using strategically designed filters allows for deep samples of emission-line galaxies at intermediate redshifts to be obtained, additional data are still needed to identify the line responsible for the detected narrowband photometric excess. Unambiguous determinations can be made with spectroscopy. However, since spectra are not usually immediately available for the selected sources, other strategies, typically based on broadband photometry and colors, are first used to deduce the nature of the excess (e.g., Fujita et al. 2003; Kodama et al. 2004; Ly et al. 2007; Shioya et al. 2008; Sobral et al. 2012). For surveys targeting intermediate redshift emission-line galaxies, such coarse filtering may be the only method available to discriminate between different line emitters, since a prohibitive investment of telescope time is still required to obtain near-IR spectroscopy for large and deep samples (e.g., Geach et al. 2008). The resulting contamination rate and incompleteness will vary depending on the depth of the photometry and number of colors available (e.g., 15-30% contamination if *Riz* selection is used to select H α emitters at $z = 0.8$; Ly et al. 2011), but will be most severe for young, blue galaxies, since the primary spectral feature providing information on the approximate redshift, the Balmer/4000 Å break, is weak or non-existent in such populations.

To address such issues, we have attempted to improve upon the basic narrowband technique. Specifically, we wish to enable the prompt identification of H α emitting galaxies at $z \sim 2$, and also provide an initial glimpse into the state of the ISM which is encoded into the rest-frame optical emission-lines. Rather than use a single narrowband filter, we have

designed a pair of filters, both of which sample dark regions of the near-IR sky spectrum, and are coupled to capture $H\alpha$ and $[OII]\lambda 3727$ over the same redshift volume. Emission-line galaxy candidates are selected through detection of a photometric excess in a filter at $2.10\ \mu\text{m}$, and $H\alpha$ emitters are then isolated through the presence of a second narrowband excess at $1.19\ \mu\text{m}$.² The $H\alpha$ line is of particular interest because its flux is a primary indicator of the instantaneous star formation rate (SFR) – the dust-corrected $H\alpha$ luminosity is directly proportional to the ionizing flux. The $[OII]$ flux has also been used as an SFR indicator, but its strength is more strongly dependent on the metallicity and the ionization state of the gas.³ The observed $[OII]/H\alpha$ ratio thus can provide a coarse combined measure of the metallicity and reddening (e.g., Nakajima et al. 2012). Furthermore, this technique yields an excellent sample of emission-line galaxies at $z=2.2$ for follow-up NIR spectroscopy, as three key lines, $[OII]$, and $H\alpha$ along with the flanking $[NII]$ lines, are already pre-selected to fall in clean windows of the OH sky spectrum.

Here, we describe the narrowband imaging in this filter pair obtained by the New $H\alpha$ Survey (J.C. Lee et al. 2012, in preparation) using the newly commissioned FourStar infrared camera (S.E. Persson et al. 2012, in preparation) at the 6.5 Magellan-Baade telescope. Initial observations are carried out over an $11' \times 11'$ area in the Cosmic Evolution Survey field (COSMOS; Scoville et al. 2007) which overlaps HST WFC3/IR and ACS coverage by the Cosmic Assembly Near-IR Deep Extragalactic Legacy Survey (CANDELS; Grogin et al. 2011; Koekemoer et al. 2011), and WFC3/IR grism observations by the 3D-HST Survey (van Dokkum et al. 2011). We take advantage of the wealth of deep, multi-wavelength imaging observations available in COSMOS to construct spectral energy distributions (SEDs), and compute photometric redshifts for the narrowband excess sources. A unique aspect of the ensemble of data used in the photometric redshift analysis is that it includes near-IR medium-band imaging through five bands from the FourStar Galaxy Evolution Survey (Z-FOURGE; I. Labbé et al. 2012, in preparation). The Z-FOURGE filter set provides a powerful complement to the New $H\alpha$ filter pair, as it was designed to locate the Balmer- or $4000\ \text{\AA}$ - breaks in galaxies at $1.5 \lesssim z \lesssim 3.5$, a range in which a significant fraction of $2.10\ \mu\text{m}$ narrowband selected emission-line galaxies are expected to lie. Together with other public datasets, photometry in 28 filters is used, spanning from the U to K_s bands ($\sim 3800\ \text{\AA}$ to $\sim 2.2\ \mu\text{m}$). With the SEDs and photometric redshifts, we examine the composition of the narrowband excess samples, and test the effectiveness of the dual narrowband technique.

²This $[OII]/H\alpha$ dual narrowband selection technique has just recently been also used by Sobral et al. (2012) to obtain a galaxy sample at $z = 1.47$. There, $[OII]$ and $H\alpha$ are detected using Subaru/Suprime-Cam imaging in NB921, and UKIRT/WFCAM imaging in “ NB_H ” ($\lambda=1.617\ \mu\text{m}$), respectively.

³See Kennicutt (1998) and Kennicutt & Evans (2012) for a review of star formation rate indicators.

The remainder of the paper is organized as follows. In Section 2, an overview of the NewH α and Z-FOURGE parent surveys is given, and the FourStar observations and data reduction is summarized. The method for selecting narrowband excess samples and identifying dual narrowband emitters is described in Section 3. Section 4 discusses the construction of SEDs, and the computation of photometric redshifts. An inventory is taken of the various detected line-emitters using the photometric redshifts and BzK colors in Section 5, and the effectiveness of the dual narrowband excess method for identifying a clean sample of $z = 2.2$ H α emitters is evaluated. In Section 6, this sample is compared with the rest-frame UV-selected $z \sim 2$ galaxies of Erb et al. (2006a,b,c) to (i) illustrate the parameter space probed by our observations relative to a well-studied sample of intermediate redshift star-forming galaxies; and (ii) test the applicability of local scaling relations used to remove the contribution of [NII] $\lambda\lambda 6548,83$ to the narrowband excess flux, and correct for dust attenuation. Initial constraints on the $z = 2.2$ H α luminosity function based on our new observations are also presented. Finally, we summarize our findings, and describe future work with the dataset in Section 7.

Throughout the paper, the standard Λ CDM cosmology with $[\Omega_\Lambda, \Omega_M, h_{70}] = [0.7, 0.3, 1.0]$ is assumed. Magnitudes are reported on the AB system. Star formation rates are computed using the Kennicutt (1998) prescription and hence assume a Salpeter IMF with mass limits of 0.1 and 100 M_\odot .

2. Observations and Data Reduction

2.1. The New H α Survey

The FourStar narrowband imaging used in this analysis has been obtained as part of the overall NewH α Survey, a program which extends searches for emission-line galaxies into the intermediate redshift universe (J.C. Lee et al. 2012, in preparation). The NewH α Survey has been designed to capture statistical samples of both luminous (but rare), and faint emission-line galaxies, by combining the near-infrared imaging capabilities of NEWFIRM (Probst et al. 2008) at the KPNO/CTIO 4-m telescopes (FoV 27'6 x 27'6) to cover large areas, and the exquisite image quality ($\sim 0''.5$ - $0''.6$ FWHM) of FourStar at the Las Campanas Magellan 6.5-m (FoV 10'8 x 10'8) to probe luminosities that are a factor of three deeper over smaller fields. Follow-up programs with GALEX, Spitzer and the Magellan-IMACS spectrograph are in various stages of progress as described in (J.C. Lee et al. 2012, in preparation) Narrowband observations at 1.19 μm with NEWFIRM are complete, and results on (i) the H α luminosity function and SFR volume density at $z = 0.8$, and (ii) the dust attenuation of $z = 0.8$ H α emitters based on Balmer decrements measured from IMACS optical spectroscopy are

reported in Ly et al. (2011) and Momcheva et al. (2012), respectively.

For both NEWFIRM and FourStar, a pair of custom narrowband filters, which sample low OH-airglow windows in the near-IR sky spectrum, has been manufactured. The bandpasses are made to fit within high atmospheric transmission regions at 1.19 and 2.10 μm which are relatively free of terrestrial sky lines over 1% in λ (Figure 1, top). The filters are sensitive to $\text{H}\alpha$ at $z=0.8$ (near the beginning of the ten-fold decline in the cosmic SFR density) and at $z=2.2$ (within the peak of the cosmic star formation history). Fortuitously, filters centered around these two wavelengths can also be designed so that both $[\text{OII}]\lambda 3727$ and $\text{H}\alpha$ emission can be detected from the same galaxies at $z = 2.2$ (Figure 2). Again, such dual narrowband excess detections help to differentiate $\text{H}\alpha$ emitters from other emission-line sources prior to confirmation with near-IR spectroscopy. Another useful feature of the particular redshift singled out by this filter pair is that $\text{Ly}\alpha$ appears at $\sim 3900 \text{ \AA}$, which is just above the blue cut-off of most optical cameras. Thus, a third narrowband can be designed to also detect $\text{Ly}\alpha$ in the same volumes, as has been done by Nakajima et al. (2012) (see also Hayes et al. 2010).

The central wavelength and FWHM of the two filters built for FourStar are 11908 \AA and 137 \AA and 20987 \AA and 208 \AA . Hereafter, we refer to these filters as NB119 and NB210, respectively.

The observational goal of the New $\text{H}\alpha$ survey’s FourStar program is to probe line luminosities that are roughly an order of magnitude fainter than the “knee” of the $\text{H}\alpha$ luminosity function at $z = 2.2$, to allow for example, robust constraints on the faint end slope to be derived. Based on measurements made by Geach et al. (2008) and Hayes et al. (2010), this depth is estimated to be around $\text{H}\alpha$ luminosities which translate into to observed SFRs of $5 M_{\odot} \text{ yr}^{-1}$ at $z \sim 2.2$, (fluxes of $\sim 1.7 \times 10^{-17} \text{ ergs s}^{-1} \text{ cm}^{-2}$). This limit can be reached in NB210 imaging with a limiting AB magnitude of ~ 23.7 . The corresponding depth required in the NB119 imaging to detect $[\text{OII}]$ for the faintest $\text{H}\alpha$ $z = 2.2$ emitters is roughly $8.5 \times 10^{-18} \text{ ergs s}^{-1} \text{ cm}^{-2}$ (25.2 AB), if it is assumed that the observed $\text{H}\alpha/[\text{OII}]$ ratio is 2. The assumption is based on spectroscopy of local star-forming galaxies. Such studies show an average ratio of ~ 2 , with values ranging between 1 and 4 for massive L^* systems, and an average of ~ 1.5 with values between 1 and 2 for lower luminosity dwarf galaxies (Jansen et al. 2001; Moustakas et al. 2006; see also Figure 8). The effectiveness of these chosen relative depths for identifying the $z = 2.2$ $\text{H}\alpha$ emitters in the NB210 excess sample is examined in Section 5.

2.2. Z-FOURGE

Z-FOURGE, the FourStar Galaxy Evolution Survey (I. Labbé et al. 2012, in preparation), is a program which aims to characterize the properties of galaxies at $z > 1$ by performing the first crucial (and often limiting) step of deriving reasonably accurate redshifts (i.e., $\sim 2\%$ in $\frac{\Delta z}{1+z}$). Ultimately, Z-FOURGE seeks to measure such redshifts for a sample of $\sim 30,000$ K_s -selected galaxies at $1.5 \lesssim z \lesssim 3.5$. The principal focus of Z-FOURGE is to investigate the red, early-type population using mass-selected samples. Since quiescent, non-active L^* galaxies at $z > 1$ are too faint for spectroscopy, Z-FOURGE’s strategy is to use a custom set of five medium-band, near-infrared filters to constrain the location of the Balmer/4000 Å break. The filters sample wavelengths between 1 to 1.8 μm , and splits the standard J and H bands into three ($J1$, $J2$, $J3$) and two (Hl , Hs) bands, respectively. A similar filter set has also been used with NEWFIRM by the NEWFIRM Medium-Band Survey (van Dokkum et al 2009; Whitaker et al. 2011).

Bandpasses for the Z-FOURGE medium-band filter set are shown together with the NewH α filter pair in Figure 1.

2.3. FourStar Observations

Pilot study observations for the NewH α and Z-FOURGE surveys were carried out during “science demonstration time” in FourStar’s first semester (2011A) on the Magellan-Baade 6.5m telescope. Both programs targeted the same region centered on $\alpha = 10^h00^m32^s.4$ $\delta = +02^\circ16'58''$, within the CANDELS-COSMOS field. Standard near-infrared observing procedures were followed. The narrowband observations are summarized here. A description of the medium-band observations can be found in the Z-FOURGE survey paper (I. Labbé et al. 2012, in preparation).

Narrowband observations were performed over a span of eight nights (24 January; 19, 21-22 February; 13-14, 19-20 March 2011), which were shared with the Z-FOURGE survey. Cumulative integration times of 9.65 and 8.39 hrs in the NB119 and NB210 filters were obtained on a single FourStar pointing. The exposure times for individual NB119 and NB210 frames were 4 and 2 minutes, respectively. The data were taken with the instrumental gain in its low noise mode (~ 1.3 e-/ADU). Semi-random dither patterns, where the spacing between adjacent frames is maximized and the pointing centers are distributed over a $27''$ box, are used. The dithers serve to bridge the $18''$ gaps between FourStar’s four 2048×2048 HAWAII-2RG detectors; enable filtering and removal of bad pixels; and perhaps most importantly, provide a measurement of the sky in each pixel for accurate sky-subtraction. The median

seeing during the observations was $0''.6$, and varied between $0''.45$ and $0''.90$. Hence, the PSF was adequately sampled by FourStar’s $0''.159$ pixels. Sky conditions were mostly photometric, although some data were taken through thin cirrus. Continuum measurements are provided by imaging in the K_s band for the NB210 data, and by the $J2$ and $J3$ bands for NB119.

A summary of the observations is given in Table 1.

2.4. FourStar Data Reduction

The FourStar data were reduced using a custom pipeline, adapted from the IDL code used for the NEWFIRM Medium-Band Survey (see Whitaker et al. 2011). The reduction follows standard, iterative (two-pass), near-infrared reduction techniques (e.g., Labbe et al. 2003) to subtract the sky background; reject artifacts; optimally weight and stack the individual frames; and is consistent with the procedures used to process the NewH α narrowband data taken with NEWFIRM (Ly et al. 2011; J.C. Lee et al. 2012, in preparation). Corrections are applied for non-linearity and geometric distortion, and flat-fielding is currently performed using twilight flats taken in each band. Comparison with independent, publicly available, broadband near-IR imaging in COSMOS shows that large-scale systematic variations in the sensitivity over the array have been reduced to $<5\%$. Photometric calibration is performed using observations of the spectrophotometric standards GD71 and GD153, and the resultant zeropoints are accurate to within $\sim 2\%$. Further optimization of the reduction and calibration is in progress.

The $3\text{-}\sigma$ limiting depths of the stacked imaging in a $1''.2$ diameter aperture are given in Table 1. A $1''.2$ diameter aperture is roughly twice the size of the PSF, and will contain 99% of light from a point source, assuming a Gaussian profile. It is the size of the aperture used to select narrowband excess sources, as described in the next section. The narrowband observations successfully achieve the NB210 target depth described in Section 2.1 (1.7×10^{-17} ergs $\text{s}^{-1} \text{cm}^{-2}$) at the $5\text{-}\sigma$ level, and surpass it at the $3\text{-}\sigma$ level. The NB119 observations reach the target depth at about the $3\text{-}\sigma$ level. Observations in the continuum bands reach flux limits which are approximately twice as deep. The limits are computed by measuring the background in a large number of random apertures.

3. Sample Selection

3.1. Selection of NB210 Excess Objects

Sources that show a significant K_s –NB210 color excess are selected as emission-line galaxy candidates. The selection procedure follows general techniques commonly used in narrowband surveys (e.g., Villar et al. 2008, Sobral. et al. 2009, Ly et al. 2011, Nakajima et al. 2011).

First, we detect sources in the NB210 image with SExtractor, using the default parameter values which require that detections have 5 adjacent pixels which are each individually above 1.2σ of the background. Exposure maps are used as weight images to avoid spurious detections in low signal-to-noise regions. A Gaussian convolution filter with a FWHM of $0''.6$ is applied to improve identification of faint, extended, objects. A total of 4865 sources are found. K_s photometry is measured for each of these NB210 detections in matched apertures using SExtractor in “dual-image” mode. As discussed in the previous section, an aperture of $1''.2$ diameter is chosen to compute the color.

Using this photometry, NB210 excess sources are then selected by requiring that:

- (i) $\Delta(K_s\text{-NB210})$, the K_s -NB210 color corrected for the median color of bright continuum objects with $-0.4 < K_s\text{-NB210} < 0.4$ and $19.0 < \text{NB210} < 21.5$, has a positive value which is significant at the 3σ level or higher (curve in Figure 3); and
- (ii) $\Delta(K_s\text{-NB210}) > 0.275$, which is five times the scatter in $\Delta(K_s\text{-NB210})$ of the sample of continuum objects defined in (i) (upper horizontal line in Figure 3). The minimum color represents a threshold in the rest-frame equivalent width of $\text{H}\alpha$ at $z = 2.2$ of 20 \AA (cf. Ly et al. 2011, eq. 11).

The selection results in a sample of 139 objects, 13 of which are undetected in the K_s -band. The objects are individually inspected on both the narrow and broad-band FourStar images, and none appear to be spurious detections. SEDs constructed from broadband photometry (Section 4) are examined to identify stars. Three stars are found and removed, reducing the NB210 excess sample to 136 objects.

3.2. Selection of Dual Narrowband Excess Emitters

To determine which NB210 excess sources are “dual emitters” (i.e., they also show a photometric excess in the NB119 filter, and are likely to be $\text{H}\alpha$ emitters at $z = 2.2$), we perform photometry on the NB119 image, and on a combined $J2$ and $J3$ (hereafter “ $J2J3$ ”)

image. The measurements are again made with SExtractor in dual-image mode, with the detection performed on the NB210 image. This produces catalogs of NB119 and $J2J3$ photometry at the locations of each of the 4865 NB210 detections.

Criteria analogous to those described in the previous section are used to select the NB119 excess sources from these catalogs. The corresponding color-magnitude diagram is given in the right panel of Figure 3. The fraction of the NB210 excess sample which also show an excess in NB119 is 30% (N=41). In both panels of Figure 3, the NB119 excess sources are enclosed with blue circles, and the NB210 excess sources with red circles; hence the points marked in both red and blue are dual emitters. All of the dual emitters are detected in the K_s -band.

3.3. Selection of NB119 Excess Objects

Following the above procedures source detection on the NB119 image and matched aperture photometry on the $J2J3$ image can also be performed to obtain an NB119 excess selected sample without reference to the NB210 data. A total of 6894 sources are detected, with 122 showing $\Delta(J2J3-NB119) > 0.21$ at at least 3σ significance (Figure 4).

4. SEDs and Photometric Redshifts

SEDs for the narrowband detected sources are constructed from the ensemble of publicly available optical broad-band and medium-band data in the COSMOS field, in combination with the Magellan-Fourstar NewH α and Z-FOURGE imaging described above. The SEDs are fit using the EAZY code (v1.1.10; Brammer et al. 2008) to derive photometric redshifts. We use the same optical dataset and a procedure similar to those in Whitaker et al. (2011), who performed a near-IR medium-band study of the COSMOS field. With EAZY, linear combination of seven template spectra, which span a broad range of galaxy ages, along with a Bayesian prior on the observed total K_s magnitude, are used to fit the observed SEDs. Based on these fits, a variety of different characteristic photometric redshifts are calculated from the probability distribution of redshifts for a given galaxy. In the analysis that follows, “ z_{peak} ,” the redshift peak in the distribution with the highest integrated probability, is adopted as the photometric redshift.

The public datasets in the COSMOS field that are included in this analysis consist of imaging in 22 filters from the U to Z bands ($\sim 3800 \text{ \AA}$ to 9000 \AA). We use data from: (1) the Deep Canada-France-Hawaii Telescope Legacy Survey (CFHTLS *ugriz*, Erben et al. 2009;

Hildebrandt et al. 2009), and (2) Subaru Suprime-Cam ($BVr'i'z'$, Taniguchi et al. 2007; and 12 medium-band filters from 4200 Å to 8200 Å, Y. Taniguchi et al. 2012, in preparation).

Combining the COSMOS optical imaging in 22 filters with FourStar near-IR imaging in 5 Z-FOURGE medium-bands, and a standard K_s filter, provides up to 28 points for each individual SED. The imaging in the various bands were all convolved to the same PSF ($1''.24$ FWHM), and photometry was measured in $1''.5$ diameter apertures. Details on the PSF matching of the imaging, and the generation of a matched multi-wavelength flux catalog are given in Spitler et al. (2012) and I. Labbe et al. (2012, in preparation).

Our photometric redshifts are in reasonable agreement with available spectroscopic redshifts for the NB210 excess sources. We searched the zCOSMOS catalog (Lilly et al. 2007) for spectroscopic redshifts, and found 4 NB210 excess emitters with matches within $1''$. All had $z_{spec} < 1$, and none were dual excess emitters. Each of the 4 galaxies have individual photometric and spectroscopic redshifts which are consistent to within 1% in $\frac{\Delta z}{1+z_{spec}}$. The NB210 excess for two galaxies can be identified as originating from Pa α at $z = 0.12$, and from HeI λ 10830 at $z = 0.94$ for the other two.

An additional check of the accuracy is also performed by comparing the photo- z 's of the larger parent sample of NB210 detections (as opposed to the NB210 *excess* detections) with available spectroscopic redshifts. There are 458 galaxies with NB210 detections that have reliable spectroscopic redshifts (zCOSMOS “confidence class” $> 90\%$) within $1''$. Comparison of the photometric and spectroscopic redshifts for $z_{spec} < 1.4$ show a dispersion of $\sigma(\frac{\Delta z}{1+z_{spec}})=0.034$, with no significant mean offset. This accuracy may appear to be low relative to the $\sim 1\%$ reported by Ilbert et al. (2009) for their own set of photo- z 's based on 30 bands of photometric data. However, the NB210 detections which have spec- z 's available in zCOSMOS are much fainter on average (the median i_{AB}^+ in a $3''$ aperture is 22 mag) than the $17.5 \leq i_{AB}^+ \leq 22.5$ sample for which the 1% photo- z 's have been derived. Photo- z 's computed by Ilbert et al. (2009) are available for 90% of the NB210 detections with spec- z 's, and when these are compared, $\sigma(\frac{\Delta z}{1+z_{spec}})=0.041$, consistent with the accuracy of the photo- z 's derived here.

5. Composition of the Narrowband Excess Samples

5.1. NB119 Excess Emitters

The photometric redshifts provide a first look at the composition of the narrowband excess samples. As expected, the photo- z distribution shows a series of peaks at redshifts where strong emission-lines appear in the filter. Figure 5 shows that the main emission-lines

detected in the FourStar NB119 excess sample (N=122) are:

- [SIII] $\lambda\lambda$ 9069,9532 at $z = 0.31$ and 0.24 ,
- [SII] $\lambda\lambda$ 6717,6731 at $z = 0.76$,
- H α at $z = 0.80$,
- [OIII] $\lambda\lambda$ 4959,5007 at $z = 1.39$ and 1.36 ,
- H β at $z = 1.44$, and
- [OII] λ 3727 at $z = 2.19$.

The majority of the sample is at $z > 1$. Roughly a quarter are [OIII] or H β emitters, while a third are [OII]. The distribution is considerably different from, but highly complementary to those of previous narrowband surveys at $1.19 \mu\text{m}$. Past studies reached half of the depth of the current observations or less, but covered larger fields, and hence were dominated by foreground H α emitters at $z \sim 0.8$ (e.g., Villar et al. 2008; Sobral et al. 2009; Ly et al. 2011). Here, H α or [SII] candidates comprise only about 10% of the sample ($N \sim 15$), but nearly all of these objects have luminosities lower than $10^{41} \text{ ergs s}^{-1}$, consistent within the expectations based on extrapolations of published H α luminosity functions at $z = 0.8$, and the volume covered in this one FourStar pointing. An H α luminosity of $10^{41} \text{ ergs s}^{-1}$ corresponds to $0.8 M_{\odot} \text{ yr}^{-1}$, and the candidates span SFRs down to $\sim 0.3 M_{\odot} \text{ yr}^{-1}$, similar to the present activity of the Large Magellanic Cloud (Whitney et al. 2008; Harris & Zaritsky 2009). Ultimately, the NewH α FourStar NB119 data will allow us to derive the most stringent constraints on the faint-end slope of the H α luminosity function, and probe the star formation properties of true dwarf galaxies at $z = 0.8$.

In principle, detection of Ly α at $z = 8.8$ with the NB119 filter is also possible, but unlikely given the expected number densities of Ly α emitting galaxies at early times, and the volume and depth probed by our data (cf., Nilsson et al. 2007; Sobral et al. 2009). If the Ly α luminosity function at $z = 6.6$ (Ouchi et al. 2010) is assumed to hold at $z = 8.8$, 0.4 Ly α emitters would be expected in one FourStar NB119 pointing with depth of $10^{-17} \text{ ergs s}^{-1} \text{ cm}^{-2}$. However, this assumption is likely to lead to an overly optimistic estimate as Ono et al. (2012) has reported that the Ly α luminosity function appears to decrease by a factor of two to three from $z \sim 6$ to 7. We are currently investigating whether any of the NB119 sources are Ly α candidates, and results will be reported in a forthcoming paper. Further discussion of the NB119 excess selected sample is deferred to future work. The remainder of this paper will focus on the NB210 excess sample, and dual NB210/NB119 excess emitters.

5.2. NB210 and Dual Narrowband Excess Emitters

In comparison, the NB210 filter is sensitive to a broader array of emission-lines. The filter will not only detect lines redward of $1.19 \mu\text{m}$ (such as $\text{Pa}\alpha$, $\text{Pa}\beta$ and all the high order Brackett lines in between), but also those in the near-IR below $1.19 \mu\text{m}$ (such as $\text{HeI}\lambda 10830$ and $\text{Pa}\gamma$) since the NB210 filter will capture these lines at higher redshift and thus probe significantly larger volumes relative to the NB119 filter. As shown in Figure 6, the main emission-lines detected in the NB210 excess sample (N=139) are:

- Brackett lines from $\text{Br}\delta$ to the series limit from $z = 0.08$ to 0.43 ,
- $\text{Pa}\alpha$ to $\text{Pa}\epsilon$ at $z = 0.12, 0.64, 0.92, 1.09, 1.20$ (series limit at $z = 1.56$),
- $[\text{FeII}]\lambda 16435$ at $z = 0.28$
- $\text{HeI } \lambda 10830$ at $z = 0.94$,
- $[\text{SIII}]\lambda\lambda 9069, 9532$ at $z = 1.31$ and 1.20 ,
- $[\text{SII}]\lambda\lambda 6717, 6731$ at $z = 2.12$,
- $\text{H}\alpha$ at $z = 2.19$,
- $[\text{OIII}]\lambda\lambda 4959, 5007$ at $z = 3.23$ and 3.19 ,
- $\text{H}\beta$ at $z = 3.31$, and
- $[\text{OII}]\lambda 3727$ at $z = 4.62$,

The majority of NB210 excess emitters are also at $z > 1$. Over a third are $\text{H}\alpha$ or $[\text{SII}]$, about a quarter are $[\text{OIII}]$ or $\text{H}\beta$, and there may possibly be a few $[\text{OII}]$ emitters in the sample. Approximately 40% are due to H or He recombination emission from galaxies in the foreground. There is also a spike at $z \sim 0.3$ containing about 15 objects, where the shock excited $[\text{Fe II}]$ line is expected to appear in the NB210 filter. As mentioned above, only four objects have spectroscopic redshifts from the zCOSMOS survey. These show that $\text{Pa}\alpha$ at $z = 0.12$ is responsible for the NB210 excess in two galaxies, and that the excess is from $\text{HeI}\lambda 10830$ at $z = 0.94$ in the other two.

The photo- z distribution of NB210 excess emitters that also have an excess in the NB119 band is shown with the shaded histogram in Figure 6. About 90% (36/41) of the dual narrowband excess emitters have photo- z 's between 1.8 and 2.6, demonstrating that the technique succeeds in identifying the $z = 2.2$ $\text{H}\alpha$ emitters in the sample. Five dual excess emitters have photo- z 's less than 0.4, but examination of their SEDs and photo- z probability distribution functions, shows that they can also be reasonably fit with models at $z = 2.2$.

The effectiveness of the NB210/NB119 dual narrowband excess technique for selecting a clean sample of $H\alpha$ at $z = 2.2$ can also be shown by plotting the objects on a BzK color-color diagram. The BzK diagram has frequently been used to obtain samples of galaxies with redshifts between about 1.4 and 2.5 with relatively high completeness and low contamination, and also to distinguish between star-forming and passively evolving galaxies, as well as stars (e.g., Daddi et al. 2004; Kong et al. 2006; McCracken et al. 2010). The method was introduced, calibrated and tested by Daddi et al. (2004) using both spectroscopic samples and stellar population synthesis models. In Figure 7, the original criteria given by Daddi et al. (2004) are marked with solid lines.⁴ All but three of the dual excess emitters (blue solid symbols) satisfy the criteria for classification as intermediate redshift star-forming galaxies. Even the three objects that fail to meet the criteria fall in a region slightly below the star-forming BzK boundary, $(z-K)-(B-z) > -0.2$, in which populations dominated by very young populations ($\lesssim 10^8$ yrs) can exist. Daddi et al. (2004) notes that to capture such galaxies, the boundary must be extended to $(z-K)-(B-z) > -0.8$ (dashed line), but that this comes at the cost of higher contamination by populations at $z < 1.4$. The five dual emitters that have photo- z 's less than 0.4 (triangles) straddle the formal $(z-K)-(B-z) > -0.2$ star-forming BzK boundary, with two falling outside the boundary. Optical spectroscopy can be performed to check whether these are in fact low redshift galaxies. In any case, the contamination of the dual excess sample with non- $H\alpha$ emitters will be very low, $\lesssim 5\%$.

Figure 6 also shows that there are NB210 excess objects that have photo- z 's which would make them $H\alpha$ candidates, but do not have NB119 excess detections. If the photo- z range for $H\alpha$ is taken to be between 1.8 and 2.6 (as defined by the range of the majority of dual excess emitters), there are nine such objects. The two most likely explanations for these objects is that the NB210 excess is due to $[SII]\lambda\lambda 6717, 31$, or that the depth of the NB119 image was not sufficient to detect $[OII]$.

To examine the latter possibility, the $H\alpha+[NII]$ and $[OII]$ fluxes for the objects in the NB210 excess sample are plotted in Figure 8, and compared with those observed locally from the Sloan Digital Sky Survey (SDSS) Data Release 7 sample (DR7; Abazajian et al. 2009). Emission-line fluxes are computed from the FourStar narrowband and broadband photometry in the usual way (e.g., see equations 9 and 10 in Ly et al. 2011). Spectroscopic emission-line fluxes for the SDSS sample are made publicly available by the MPA/JHU group⁵. The fluxes

⁴The empirically derived transformation given by McCracken et al. (2010) to account for differences between the Subaru B_J filter used to image the COSMOS field, and the B -VLT filter used by Daddi et al. (2004) is applied to the data shown.

⁵<http://www.mpa-garching.mpg.de/SDSS/DR7/>

have been extracted from Gaussian fits to the line profiles, where the continuum has been subtracted using a best-fit model generated by a combination of simple stellar population at various ages from the Bruzual & Charlot spectral synthesis code (Bruzual & Charlot 2003). Corrections for Galactic foreground reddening are applied. SDSS spectra for a total of 818,333 galaxies at $z < 0.7$ are available, but here we only consider the sub-sample of $\sim 60,000$ star-forming galaxies with $0.005 < z < 0.22$ (following Brinchmann et al. 2004) and an empirically estimated fiber aperture correction less than 2. The 3σ sensitivities of the narrowband imaging to these lines is also illustrated by indicating which of the SDSS galaxies would be detectable if they were instead at $z = 2.2$. Clearly, *if* the full range of local galaxies exists at redshift of two, current near-IR narrowband surveys, of which NewH α is one of the most sensitive to faint line emission, would still only be able to probe the most luminous H α and [OII] emitters.

In Figure 8, all of the dual narrowband excess emitters lie in the region above both the NB119 and NB210 3σ line flux sensitivity limits as expected (yellow region). The region where objects would be only detected with a NB210 excess is indicated in cyan. Here, more uncertain NB119 excess fluxes (which would correspond to [OII] if the objects were indeed at $z = 2.2$) down to the 1σ limit (marked by the row of upper-limit symbols) are also plotted. It is clear that even without additional photo-z or SED information, some objects can be eliminated as H α candidates because they would have [OII]/H α ratios that are unphysical. However, the nine galaxies that do not have 3σ excess detections in NB119, but yet have photo-z's which would make them H α candidates, all would have [OII]/H α ratios that fall within the range of physically plausible values. Further, all except one have nominal NB119 excess detections above 1σ , which would not be expected if the NB210 excesses were mostly due to [SII]. This suggests that the majority of these objects are H α emitters at $z = 2.2$. Therefore, the dual narrowband technique, as implemented here, is estimated to identify $\gtrsim 80\%$ of $z = 2.2$ H α emitters detected in the NB210 excess sample. Near-IR spectroscopy will be required to confirm this success rate.

6. Constraints on the H α Luminosity Function at $z = 2.2$

With a clean, complete sample of H α emitters in hand, constraints on the $z = 2.2$ H α luminosity function can be computed. We follow the procedures discussed in detail in Ly et al. (2011), which presents our results on the H α luminosity function at $z = 0.8$, using NB119 imaging taken with the much wider FoV NEWFIRM camera on the KPNO 4m telescope. Here, we outline the procedure, pointing out differences between the analyses when they arise.

The key steps include (1) transforming the narrowband photometric excesses into dust-corrected $H\alpha$ luminosities; (2) computing the effective volume of the observations; (3) estimating and applying completeness corrections; and (4) fitting a function, usually that of Schechter (1976) (but see Salim et al. 2012, in preparation), to model the distribution. The step where methods which have been previously applied for analogous studies at lower redshifts cannot be directly transplanted for the current analysis is the first one.

To compute the intrinsic $H\alpha$ luminosity from the narrowband excess, two main corrections are required, one for emission from $[NII]\lambda\lambda 6548,83$ (since the flux from these lines will contribute to the narrowband excess as $R\sim 100$ filters are generally used), and another for dust attenuation within the galaxy. Because measurements of $[NII]/H\alpha$ and $A(H\alpha)$ ⁶ are not immediately available for the individual members of a sample, coarse empirical scaling relationships calibrated on local samples such as the SDSS have been employed to estimate their values (e.g., Villar et al. 2008; Sobral et al. 2009; Lee et al. 2009; Ly et al. 2011). For example, in previous $H\alpha$ narrowband studies, relations providing $[NII]\lambda 6584/H\alpha$ as a function of the rest-frame $H\alpha$ equivalent width (Villar et al. 2008), and the intrinsic $H\alpha$ luminosity as a function of the observed $H\alpha$ luminosity (Hopkins et al. 2001) have been used. However, it is well known that such relationships have scatters of a factor of two or more (e.g., Villar et al. 2008; Kennicutt et al. 2008; Lee et al. 2009; Momcheva et al. 2012). Moreover, it is unclear whether these scaling relations will be valid at $z = 2$, as the gas metallicities and dust reddenings of galaxies of a given stellar mass are known to decrease with increasing redshift (Erb et al. 2006a; Reddy et al. 2006; Maiolino et al. 2008; Reddy 2010).

Though we do not yet have independent measurements of $[NII]/H\alpha$ and $A(H\alpha)$ for our $z = 2.2$ $H\alpha$ sample, we can take a first look at where these values are likely to lie via comparison to the well-studied rest-frame UV-selected $z \sim 2$ sample of Erb et al. (2006a,b,c), for which $H\alpha$ spectroscopy has been obtained, and dust reddenings have been computed both from SED fitting and the UV continuum slope (Erb et al. 2006c). Such an exercise also serves to place the current dataset in the more familiar context of a broadly referenced sample of star-forming galaxies at $z \sim 2$.

In Figure 9, the rest-frame equivalent width, and the line luminosity, scaled by 7.9×10^{-42} to give approximate star formation rates (Kennicutt 1998), are plotted against the K_s magnitude for both samples. For the UV-selected sample, the measurements are made from slit spectroscopy, and so are for only the $H\alpha$ line. These measurements include a factor of two correction to account for slit losses, as determined by Erb et al. (2006c). For the FourStar

⁶attenuation of $H\alpha$ emission in magnitude units

$H\alpha$ emitters, the plotted values include contributions from both [NII] and $H\alpha$. No dust corrections have been applied to either sample. K_s magnitudes on the AB scale are shown for both, where $K_s [AB]=K_s [Vega]+1.83$ is applied to the Erb data.

Although the EW range (and hence range of specific SFR) spanned by the two samples are similar, it is clear that the $H\alpha$ emitters probe SFRs and continuum luminosities (and hence stellar masses) that are significantly lower than the UV selected sample. The medians of the distributions for both quantities are at least a factor of two smaller for the $H\alpha$ emitters. Hence, if the [NII]/ $H\alpha$ values and reddenings derived for the UV-selected sample were to be used to formulate corrections for the $H\alpha$ emitters, it seems that some extrapolation of the corrections would be required.

We first examine the reddenings for the UV-selected sample found by Erb et al. (2006b) in the left panel of Figure 10. Here, $A(H\alpha)$ is plotted as a function of the observed SFR, to enable comparison with the locally calibrated Hopkins et al. (2001) relation. Erb et al. (2006b) provide $E(B-V)$'s derived by SED fitting, and these are scaled using the Calzetti et al. (2000) extinction law to give the attenuation in $H\alpha$. $A(H\alpha)$ is computed both by assuming that the reddening in the gas is about twice that of the stars, which is found locally (Calzetti 2000); and, that it the same as that of the stars, which seems to be supported by intermediate redshift observational studies (Erb et al. 2006b, but see Forster-Schreiber et al. 2009). There is no correlation with the observed SFR, and in both cases, the Hopkins prescription over-predicts the attenuation. The median $H\alpha$ attenuation is 0.5 mag when $E(B-V)_{stars}=E(B-V)_{gas}$ is assumed, and so for the current analysis, we simply adopt this fixed value to perform the dust correction.

Next, in the right panel of Figure 10, the equivalent widths from Erb et al. (2006c) are used to predict $[NII]\lambda 6584/H\alpha$ using the local relation of Villar et al. (2008). The estimates are plotted as a function of K_s magnitude. This enables comparison with the Erb et al. (2006a) measurements, which were performed on long-slit spectra, stacked in bins of stellar mass. K_s magnitudes are provided for each mass bin. Figure 10 shows that the local relation actually yields reasonable predictions, albeit with large scatter. The consistency between the locally-based estimates and the $z \sim 2$ measurements may initially seem surprising given the known evolution of the mass-metallicity relation, but is likely a consequence of the ‘‘Fundamental Metallicity Relation,’’ or FMR, proposed by Mannucci et al (2010). The FMR is a more general relation between mass, SFR and metallicity, with a small residual dispersion in the metallicity of only $\sim 12\%$ based upon the SDSS, and is shown to hold for galaxies to $z \sim 2.5$. Collapse in one dimension yields a correlation between metallicity and specific SFR, which is traced by the $H\alpha$ EW. Here, although the Villar et al. (2008) scaling relation appears to be valid, we choose to use a linear fit to the Erb et

al. (2006c) measurements to estimate the $[\text{NII}]\lambda 6584/\text{H}\alpha$ values for the $\text{H}\alpha$ emitters from their K_s magnitudes. The fit is given by $[\text{NII}]\lambda 6584/\text{H}\alpha = -0.15K_s + 3.67$. For $K_s > 23.3$, $[\text{NII}]\lambda 6584/\text{H}\alpha = 0.04$ is assumed. The validity of both this relation and the 0.5 mag dust correction will need to be tested in the future with follow-up near-IR spectroscopy.

Steps (2), (3), and (4) are then performed by following the methods used in Ly et al. (2011), which we briefly review here. The effective volume is computed, accounting for the deviation of the filter profile from a perfect top-hat function. The maximum surveyed volume is $3.83 \times 10^5 \text{ Mpc}^3 \text{ deg}^{-2}$ for $\text{H}\alpha$ emission-line fluxes above $2.7 \times 10^{-17} \text{ erg cm}^{-2} \text{ s}^{-1}$, and decreases to half of this volume at an $\text{H}\alpha$ emission-line flux of $1.35 \times 10^{-17} \text{ erg cm}^{-2} \text{ s}^{-1}$. The total area covered by the stacked narrowband observations is 127 arcmin^{-2} , and hence the resulting maximum volume is $1.36 \times 10^4 \text{ Mpc}^3$. Next, Monte Carlo simulations are performed to estimate the completeness fraction at a given $\text{H}\alpha$ luminosity. The simulations are used to compute the probability of detecting a source of a given continuum brightness and emission-line flux (i.e., NB210 excess), based upon the sensitivity of the narrow and broad-band images. We follow a maximum-likelihood approach where assumptions about the true distributions of the $z \sim 2$ star-forming population are varied to best reproduce the observed $\text{H}\alpha$ LF and EW distribution. To model the intrinsic $\text{H}\alpha$ EWs, log-normal Gaussian distributions are adopted, where the *rest-frame* median logarithmic EW and standard deviation are varied in 0.1 dex increments between 1.8 and 2.3; and 0.1 and 0.6, respectively. The K_s -band luminosity function for $z \sim 2$ star-forming BzK galaxies, which is determined from data published in Ly et al. (2011b), is assumed. With the K_s -band brightnesses and $\text{H}\alpha$ EW's, 400,000 sources for each of 6×6 different EW model distribution are generated. Noise is then added to the sources, and the selection criteria described in Section 5.2 are applied to calculate the completeness as a function of $\text{H}\alpha$ flux. The EW model that best reproduces both the observed $\text{H}\alpha$ LF and EW distribution is described by a median $\log(\text{EW}_{rest})$ of 2.1 and $\sigma[\log(\text{EW})] = 0.3$ dex. The completeness of the sample is 99% at a flux of $2.2 \times 10^{-17} \text{ ergs s}^{-1} \text{ cm}^{-2}$ and 50% at $1.2 \times 10^{-17} \text{ ergs s}^{-1} \text{ cm}^{-2}$. For comparison, the median $\log(\text{EW}_{rest})$ is 1.5 for local galaxies along the star-forming sequence (Lee et al. 2007). The characteristic specific SFR, which is traced by $\text{EW}(\text{H}\alpha)$, is a factor of ~ 3 higher at $z \sim 2$ (c.f., Noeske et al. 2007).

Figure 11 presents the $\text{H}\alpha$ luminosity functions. The left panels show the LFs based on the dual narrowband excess selected sample (N=41), while the LFs in the right panels also include the NB210 excess galaxies with photo- z 's between 1.8 and 2.6 (N=50). In every plot, there are two sets of points corresponding to (1) the raw $\text{H}\alpha + [\text{NII}]$ luminosities, and (2) the fully-corrected luminosities, where the contribution of the $[\text{NII}]$ lines, 0.5 mag of dust attenuation, and survey incompleteness have all been taken into account. The data points for all four luminosity functions are given in Table 2. The bottom row is identical to the top

row, except that the results of Hayes et al. (2010; hereafter H10) and Sobral et al. (2012; hereafter S12) are overplotted.

Both the raw and fully-corrected LFs appear to rise steeply at the faint end. Single power-law fits to the faintest three, four or five bins for the four samples shown in Figure 11 yield power law exponents in the range $-1.60 \leq \alpha \leq -1.93$, with 1σ uncertainties of ~ 0.3 . These values are consistent with the H10 VLT/HAWK-I result of $\alpha = -1.77 \pm 0.21$, which was based on a photometric redshift selected $2.095 \mu\text{m}$ narrowband excess sample ($N=55$). Such results may imply that the star formation rate distribution function gradually steepens from the present day value of $\alpha = -1.2 \pm 0.2$ (e.g. Perez-Gonzalez et al. 2003), as has been suggested previously (e.g., Hopkins et al. 2000; Reddy & Steidel 2009; H10; but see S12), though the uncertainties are still too large to conclude that evolution in α occurs. Robust measurements of this evolution will provide insight into hierarchical mass assembly through gas-rich mergers, and the regulation of star formation in low-mass halos.

Of course, however, the value of α given by the power-law fit is an upper-limit. How closely this approximates the true value depends on how far the data points are from L^* , the knee of the LF. Given the volume probed by our observations, and previous estimates of $L^* = 10^{43.07 \pm 0.22}$ ergs s^{-1} (H10; uncorrected for dust), it is clear that the current FourStar data do not provide useful constraints on the bright, exponential end. A complete determination of the $z = 2.2$ $\text{H}\alpha$ LF from the New $\text{H}\alpha$ survey awaits the integration of wide-shallow data from NEWFIRM observations (C. Ly et al. 2012, in preparation). However, initial comparisons can be made with the recent study of S12, who combine VLT/HAWK-I and UKIRT/WFCAM imaging in the standard H_2 narrowband filter at $2.121 \mu\text{m}$, and select their $\text{H}\alpha$ emitters with a mix of photometric redshift, BzK , and UBR selection criteria ($N=45$ and 518 , for the HAWK-I and WFCAM observations respectively). The bottom panels of Figure 11 show that, despite the patchwork of selection methods applied by S12, there is good agreement between the two studies at the faint end of the fully-corrected LF datapoints. S12 report $\alpha = -1.57 \pm 0.2$ with their additional data covering higher luminosities, as they find a relatively low L^* of $10^{42.66 \pm 0.1}$ ergs s^{-1} (for 0.5 mag attenuation and α fixed at -1.6). If the FourStar datapoints are combined with those from the S12 UKIRT/WFCAM imaging, the best fit Schechter parameters are $L^* = 10^{42.64 \pm 0.21}$ ergs s^{-1} , $\log(\phi^*) = -2.70 \pm 0.30$ and $\alpha = -1.58 \pm 0.40$.

7. Summary and Future Work

In this paper, we have presented first results from near-infrared narrowband imaging observations with the new FourStar camera at the 6.5m Magellan telescope. We have shown

that our implementation of the dual narrowband technique for isolating deep intermediate redshift emission-line selected samples is highly effective, and identifies the $z = 2.2$ H α emitters our NB210 excess sample with $\gtrsim 80\%$ completeness. The dataset is the deepest of its kind: the exquisite image quality ($\sim 0''.55$ FWHM) resulting from the combination of instrument, telescope and site results in $1.19 \mu\text{m}$ and $2.10 \mu\text{m}$ imaging which probe 3σ emission-line depths down to $1.0 \times 10^{-17} \text{ erg s}^{-1} \text{ cm}^{-2}$ and $1.2 \times 10^{-17} \text{ erg s}^{-1} \text{ cm}^{-2}$ respectively, and is competitive with recent HAWK-I narrowband observations at the 8.2m VLT (e.g., Hayes et al. 2010). Our $z = 2.2$ H α sample extends the luminosities and SFRs probed by the well-studied UV-selected $z \sim 2$ galaxies of Erb et al. (2006c) by a factor of at least two. Optimization of the data reduction and analysis will further enable us to increase the depth of the sample by up to 40%.

We compute constraints on the faint-end slope of the $z = 2.2$ H α luminosity function using both the dual narrowband selected H α emitters (N=41), and a combined sample of dual narrowband and photometric redshift selected galaxies (N=50). Fitting of a pure power-law gives an upper-limit on α of -1.85 ± 0.31 , which is steeper than other recent estimates based on coarser selection techniques, but consistent within the large uncertainties that currently characterize such measurements. Combining our LF points with those at higher luminosities from other work, the slope decreases to $\alpha = -1.58 \pm 0.40$. Additional data recently obtained from an FourStar pointing targeting the CANDELS area in the CDF-S will enlarge the sample, and tighten this constraint.

These “narrow-deep” FourStar observations have been obtained as part of the larger NewH α Survey, which will combine the data with “wide-shallow” imaging through a similar narrowband filter pair with NEWFIRM at the KPNO/CTIO 4m telescopes, to carry out a statistical study of both luminous (but rare) and faint emission-line galaxies in the intermediate redshift universe. The dataset, in combination with the wealth of multiwavelength observations available in the extragalactic deep fields targeted, form the basis for follow-up studies on the physical properties (morphologies, dust, metallicities, recent star formation histories and stellar populations) of star-forming galaxies at a critical phase in their evolution. The FourStar observations, in particular, enable study of lower mass members of the population, even probing SFRs down to LMC-type activities of a few tenths at $z \sim 0.8$.

This project, including the purchase of the custom narrowband filters, was made possible through the support of Hubble and Carnegie Fellowships awarded to JCL. Special thanks are due to the FourStar instrument team and Carnegie Observatories, whose dedicated, long-term efforts to build an exceptional camera have enabled the science imagined for over a decade.

We thank Ryan Quadri and Rik Williams for useful discussions on using the EAZY photometric redshift code, and Gabe Brammer for providing the most recent version of the code. Helpful discussions with Ranga-Ram Chary about the application of extinction curves, with Peter Capak about luminosity functions, and with Dan Kelson about aspects of FourStar data reduction are acknowledged.

REFERENCES

- Abazajian, K. N., Adelman-McCarthy, J. K., Agüeros, M. A., et al. 2009, *ApJS*, 182, 543
- Brammer, G. B., van Dokkum, P. G., & Coppi, P. 2008, *ApJ*, 686, 1503
- Brinchmann, J., Charlot, S., White, S. D. M., et al. 2004, *MNRAS*, 351, 1151
- Bruzual, G., & Charlot, S. 2003, *MNRAS*, 344, 1000
- Calzetti, D., Armus, L., Bohlin, R. C., et al. 2000, *ApJ*, 533, 682
- Daddi, E., Cimatti, A., Renzini, A., et al. 2004, *ApJ*, 617, 746
- Erb, D. K., Steidel, C. C., Shapley, A. E., et al. 2006, *ApJ*, 647, 128
- Erb, D. K., Steidel, C. C., Shapley, A. E., et al. 2006, *ApJ*, 646, 107
- Erb, D. K., Shapley, A. E., Pettini, M., et al. 2006, *ApJ*, 644, 813
- Erben, T., Hildebrandt, H., Lerchster, M., et al. 2009, *A&A*, 493, 1197
- Fujita, S. S., Ajiki, M., Shioya, Y., et al. 2003, *ApJ*, 586, L115
- Geach, J. E., Smail, I., Best, P. N., Kurk, J., Casali, M., Ivison, R. J., & Coppin, K. 2008, *MNRAS*, 388, 1473
- Grogin, N. A., Kocevski, D. D., Faber, S. M., et al. 2011, *ApJS*, 197, 35
- Harris, J., & Zaritsky, D. 2009, *AJ*, 138, 1243
- Hayes, M., Schaerer, D., Ostlin, G. 2010, *A&A*, 509, L5
- Hayes, M., et al. 2010, *Nature*, 464, 562
- Hopkins, A. M., Connolly, A. J., Haarsma, D. B., & Cram, L. E. 2001, *AJ*, 122, 288
- Ilbert, O., Capak, P., Salvato, M., et al. 2009, *ApJ*, 690, 1236

- Jansen, R. A., Franx, M., & Fabricant, D. 2001, *ApJ*, 551, 825
- Kennicutt, R. C., Jr. 1998, *ARA&A*, 36, 189
- Kennicutt, R. C., Jr., Lee, J. C., Funes, S. J., José G., Sakai, S., & Akiyama, S. 2008, *ApJS*, 178, 247
- Kodama, T., Balogh, M. L., Smail, I., Bower, R. G., & Nakata, F. 2004, *MNRAS*, 354, 1103
- Koekemoer, A. M., Faber, S. M., Ferguson, H. C., et al. 2011, *ApJS*, 197, 36
- Labbé, I., Franx, M., Rudnick, G., et al. 2003, *AJ*, 125, 1107
- Lee, J. C., Gil de Paz, A., Tremonti, C., et al. 2009, *ApJ*, 706, 599
- Lee, J. C., Kennicutt, R. C., Funes, S. J., José G., Sakai, S., & Akiyama, S. 2007, *ApJ*, 671, L113
- Lilly, S. J., Le Fèvre, O., Renzini, A., et al. 2007, *ApJS*, 172, 70
- Ly, C., Lee, J. C., Dale, D. A., Momcheva, I., Salim, S., Staudaher, S., Moore, C. A., & Finn, R. 2011, *ApJ*, 726, 109
- Mannucci, F., Cresci, G., Maiolino, R., Marconi, A., & Gnerucci, A. 2010, *MNRAS*, 408, 2115
- McCracken, H. J., Capak, P., Salvato, M., et al. 2010, *ApJ*, 708, 202
- Moustakas, J., Kennicutt, R. C., Jr., & Tremonti, C. A. 2006, *ApJ*, 642, 775
- Nakajima, K., Ouchi, M., Shimasaku, K., et al. 2012, *ApJ*, 745, 12
- Noeske, K. G., Faber, S. M., Weiner, B. J., et al. 2007, *ApJ*, 660, L47
- Ono, Y., Ouchi, M., Mobasher, B., et al. 2012, *ApJ*, 744, 83
- Ouchi, M., Shimasaku, K., Furusawa, H., et al. 2010, *ApJ*, 723, 869
- Nilsson, K. K., Orsi, A., Lacey, C. G., Baugh, C. M., & Thommes, E. 2007, *A&A*, 474, 385
- Reddy, N. A., Erb, D. K., Pettini, M., Steidel, C. C., & Shapley, A. E. 2010, *ApJ*, 712, 1070
- Reddy, N. A., Steidel, C. C., Pettini, M., et al. 2008, *ApJS*, 175, 48
- Schechter, P. 1976, *ApJ*, 203, 297

- Shioya, Y., Taniguchi, Y., Sasaki, S. S., et al. 2008, ApJS, 175, 128
- Spitler, L. R., Labbé, I., Glazebrook, K., et al. 2012, ApJ, 748, L21
- Sobral, D., Best, P. N., Matsuda, Y., et al. 2012, MNRAS, 420, 1926
- Sobral, D., Best, P. N., Geach, J. E., et al. 2009, MNRAS, 398, 75
- Scoville, N., Aussel, H., Brusa, M., et al. 2007, ApJS, 172, 1
- Taniguchi, Y., Scoville, N., Murayama, T., et al. 2007, ApJS, 172, 9
- Taniguchi, Y., Shioya, Y., Ajiki, M., et al. 2003, Journal of Korean Astronomical Society, 36, 123
- Teplitz, H. I., Malkan, M., & McLean, I. S. 1998, ApJ, 506, 519
- Tresse, L., Maddox, S. J., Le Fèvre, O., & Cuby, J.-G. 2002, MNRAS, 337, 369
- van Dokkum, P. G., et al. 2009, PASP, 121, 2
- Villar, V., Gallego, J., Pérez-González, P. G., et al. 2008, ApJ, 677, 169
- Whitaker, K. E., et al. 2011, ApJ, 735, 86
- Whitney, B. A., Sewilo, M., Indebetouw, R., et al. 2008, AJ, 136, 18

Facilities: Magellan:Baade (FourStar), Subaru (Suprime-Cam)

Table 1. FourStar Observations for $\alpha = 10^h00^m32^s.4$ $\delta = +02^\circ16^m58^s$

Filter	Int. Time (hours)	FWHM (")	3- σ Depth (AB, in 1".2 aperture)
NB119	9.65	0.56	25.1
NB210	8.39	0.53	24.2
<i>J</i> 2	7.16	0.61	26.0
<i>J</i> 3	8.36	0.60	25.7
<i>K</i> _s	5.82	0.51	25.0

Table 2. H α Luminosity Functions at $z = 2.2$

log L	$\Phi(L)$	N	log L	$\Phi(L)$	N
Dual emitters (N=41)					
Raw			Corrected		
41.77	6.838E-03 \pm 3.419E-03	4	41.94	8.096E-03 \pm 2.649E-03	9
41.90	5.861E-03 \pm 1.566E-03	14	42.10	5.027E-03 \pm 1.451E-03	12
42.10	4.058E-03 \pm 1.223E-03	11	42.30	4.429E-03 \pm 1.278E-03	12
42.30	2.582E-03 \pm 9.760E-04	7	42.50	2.214E-03 \pm 9.038E-04	6
42.50	1.476E-03 \pm 7.378E-04	4	42.70	7.378E-04 \pm 5.217E-04	2
42.70	3.689E-04 \pm 3.689E-04	1			
Dual emitters + photo-z selected (N=50)					
Raw			Corrected		
41.74	5.569E-03 \pm 2.274E-03	6	41.93	1.021E-02 \pm 3.005E-03	11
41.90	7.966E-03 \pm 1.878E-03	18	42.10	6.703E-03 \pm 1.675E-03	16
42.10	4.427E-03 \pm 1.278E-03	12	42.30	4.798E-03 \pm 1.330E-03	13
42.30	2.951E-03 \pm 1.043E-03	8	42.50	2.952E-03 \pm 1.044E-03	8
42.50	1.844E-03 \pm 8.248E-04	5	42.70	7.378E-04 \pm 5.217E-04	2
42.70	3.689E-04 \pm 3.689E-04	1			

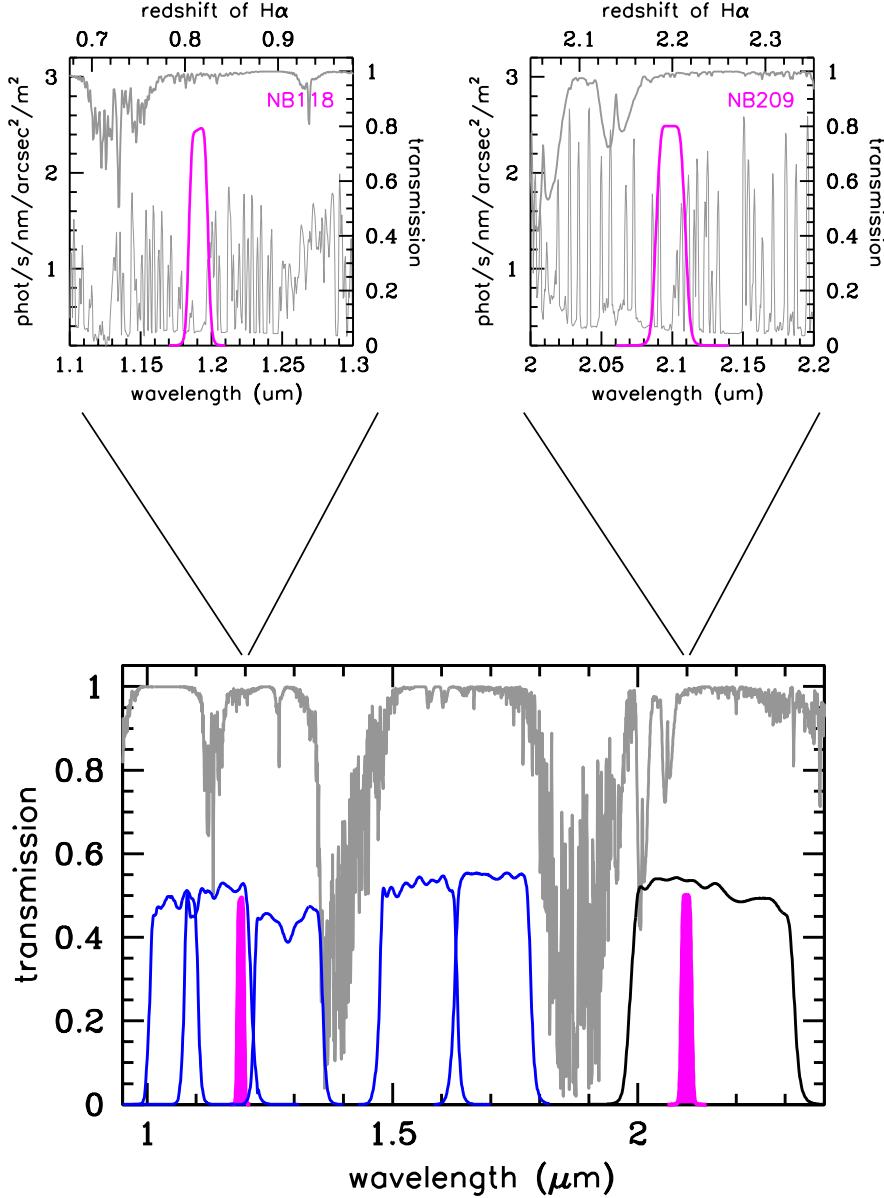


Fig. 1.— Bandpasses of the NewH α narrowband filter pair (magenta) together with those for the Z-FOURGE medium-band filter set (blue), and the standard K_s broadband (black), which are used in FourStar. The atmospheric transmission is also plotted (gray). The expanded view shows the profiles for the narrowbands overlapped on the OH sky spectrum (gray). Similar sets of filters are also used in the NEWFIRM camera. The narrowband filters probe low OH airglow regions in the sky spectrum, and are sensitive to H α at $z = 0.8$ (near the beginning of the ten-fold decline in the cosmic SFR density) and at $z = 2.2$ (within the peak of the cosmic star formation history). Sky spectrum and atmospheric transmission data from Gemini Observatories. Filter transmission data (shown in the upper plots) from Barr Associates. FourStar/Magellan system throughputs (shown in the lower plot) from S.E. Persson et al. 2012, in preparation.

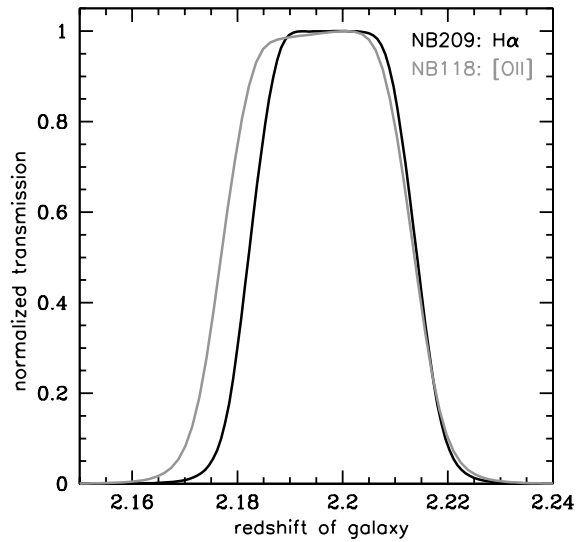


Fig. 2.— The NewH α narrowband filters are coupled such that the [OII] emission of H α emitters selected with NB210 observations can be captured by the NB119 filter. The redshift ranges over which the filters are sensitive to [OII] and H α in the same volume are illustrated in this Figure. Bandpass shifting over the field-of-view of the detector is not significant because of the positioning of the filters near the focal plane in the camera. The relative shift between the center and the corner of the field has been computed to be -6.10\AA for NB119, and -5.49\AA for NB210, which are 6% and 2.6% of the bandpass widths of the two filters. The redshift range over which NB119 is sensitive to [OII] completely encloses the range where NB210 will detect H α .

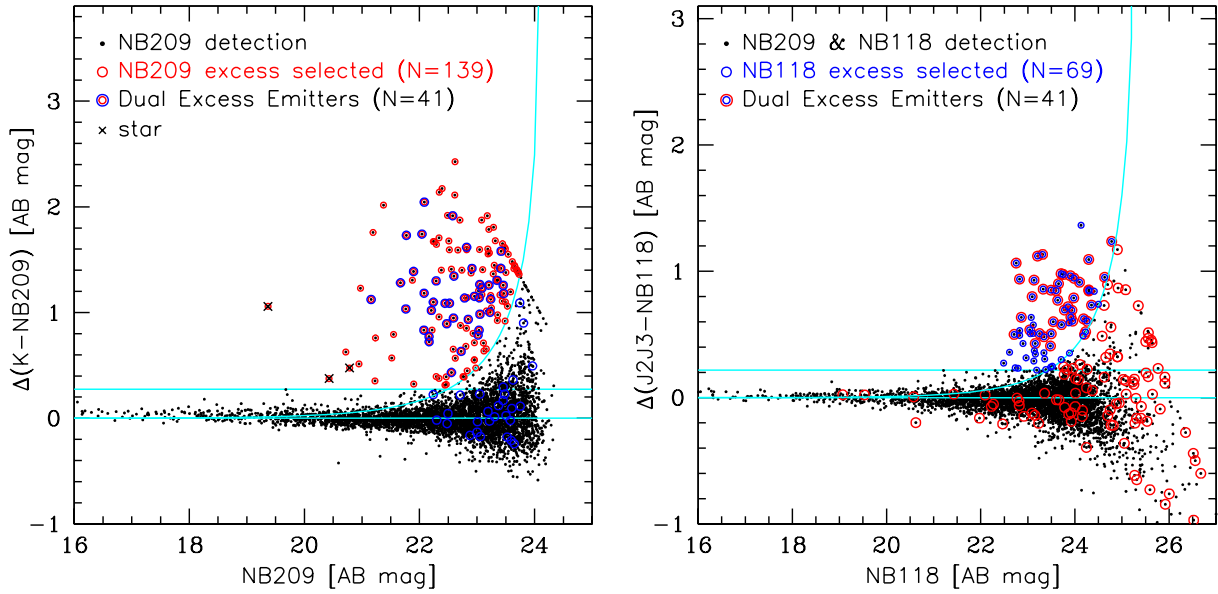


Fig. 3.— Color-magnitude diagrams illustrating the selection of NB210 excess (left panel), and *NB210-detected*, NB119 excess (right panel) sources, where the photometry has been measured in $1''.2$ diameter apertures. The upper horizontal line indicates values which are five times the scatter in the color for continuum objects with magnitudes between 19.0 and 21.5. The curves indicate the values of the color excess that are significant at the $3\text{-}\sigma$ level. In both panels, the NB119 excess sources are marked with blue circles, and the NB210 excess sources with red circles; hence the “dual emitters” are marked in both red and blue. Three stars (black crosses) are identified via inspection of SEDs constructed from broadband photometry. 30% of the NB210 excess sources are dual emitters.

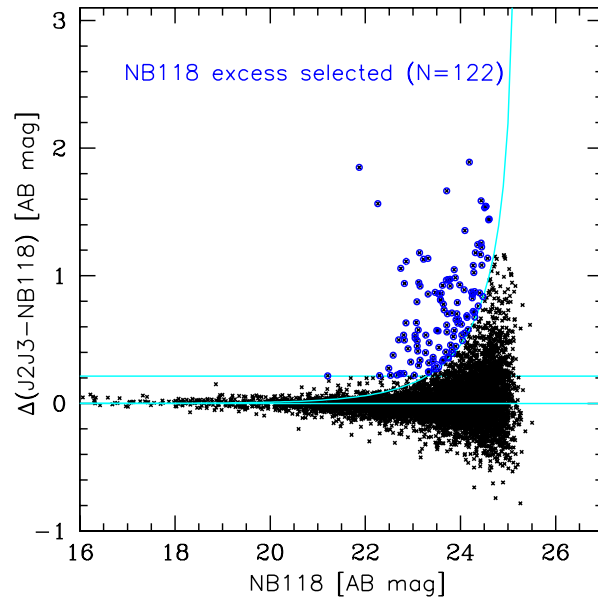


Fig. 4.— Color-magnitude diagram illustrating the selection of a NB119 excess sample. Whereas the NB119 color-magnitude diagram in Figure 3 shows photometry only at locations where there are NB210 detections, in this Figure, all sources detected on the NB119 image are plotted. Again, the photometry has been measured in $1''.2$ diameter apertures; the upper cyan horizontal line indicates values which are five times the scatter in the color for continuum objects with magnitudes between 19.0 and 21.5; and the curve indicates values of the color excess that are significant at the $3\text{-}\sigma$ level.

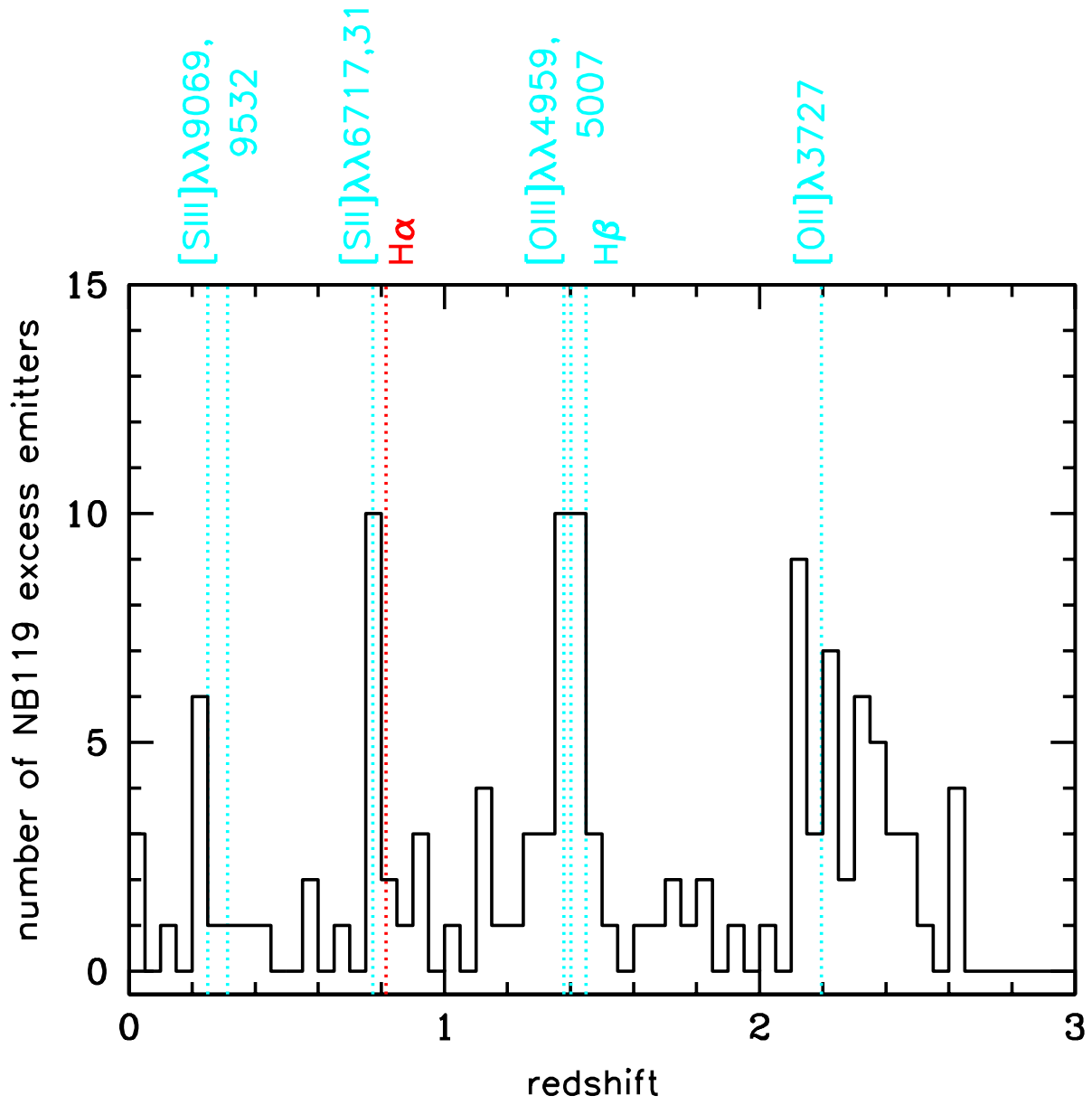


Fig. 5.— Distribution of photometric redshifts for the NB119 excess selected sample.

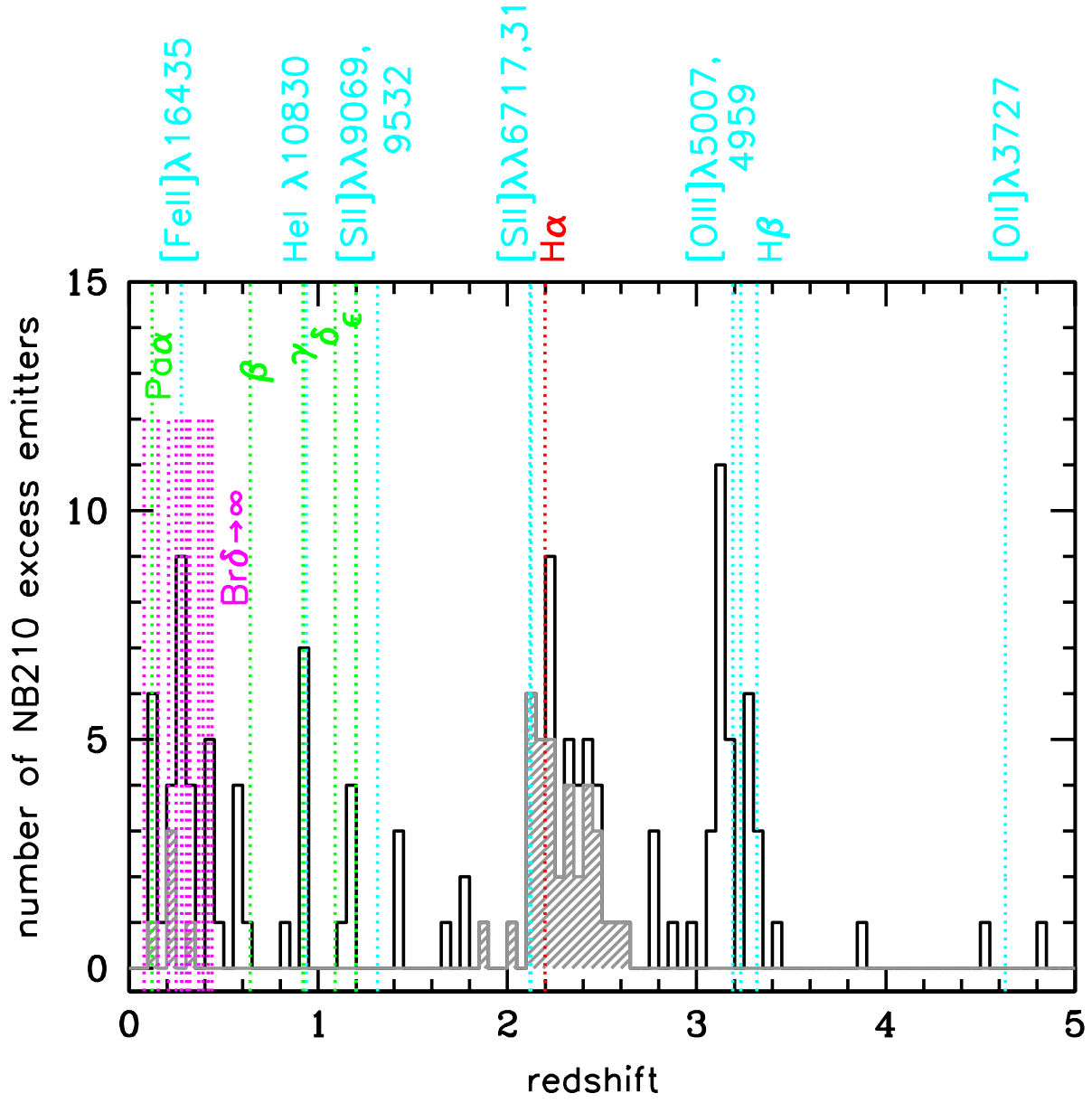


Fig. 6.— Distribution of photometric redshifts for the NB210 excess selected sample. Dual NB210/NB119 excess emitters are shaded.

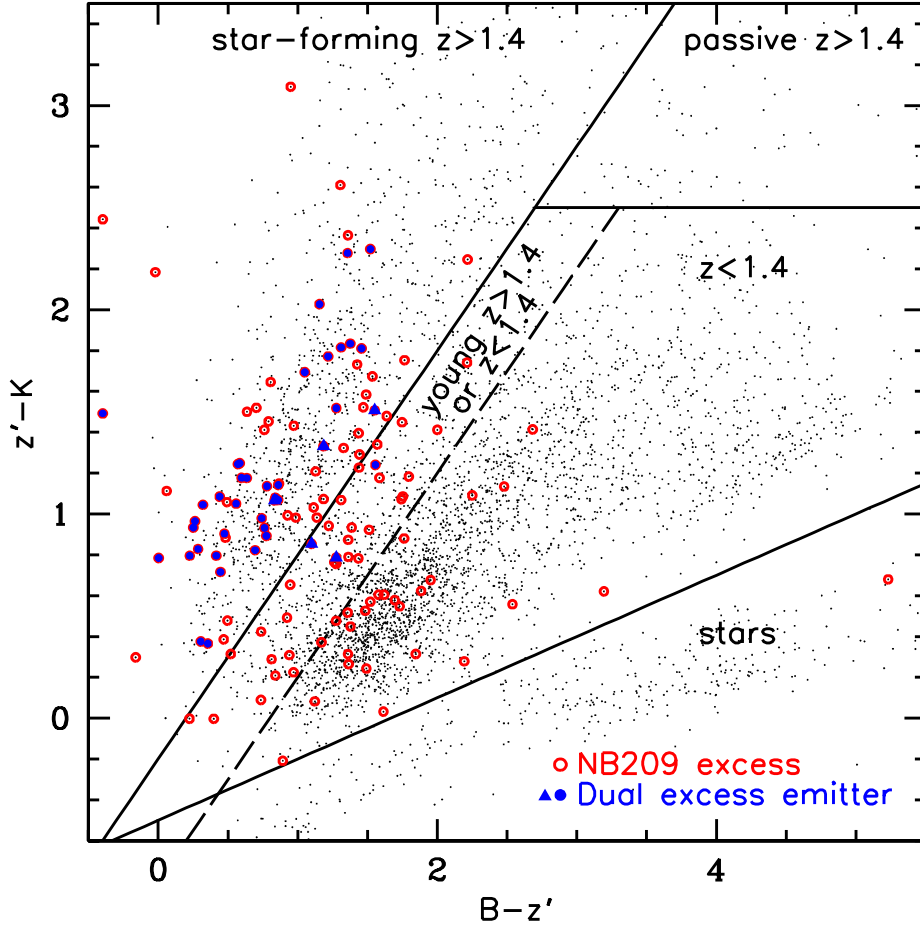


Fig. 7.— A BzK color-color diagram for all objects detected in the NB210 imaging. NB210 excess selected objects and dual NB210/NB119 excess emitters are marked as indicated in the figure. Criteria used to distinguish different populations of galaxies as given by Daddi et al. (2004) are also shown. The dual excess emitters nearly all satisfy the criteria for classification as “ $sBzK$ ” galaxies, indicating that they are star-forming galaxies at redshifts between 1.4 and 2.5, and demonstrating that the dual excess selection technique succeeds in identifying the $z = 2.2$ $H\alpha$ emitters in the sample. Five dual excess emitters have photo- z ’s less than 0.4 (blue triangles), but their SEDs can also be reasonably fit with models at $z = 2.2$, as corroborated by their BzK colors.

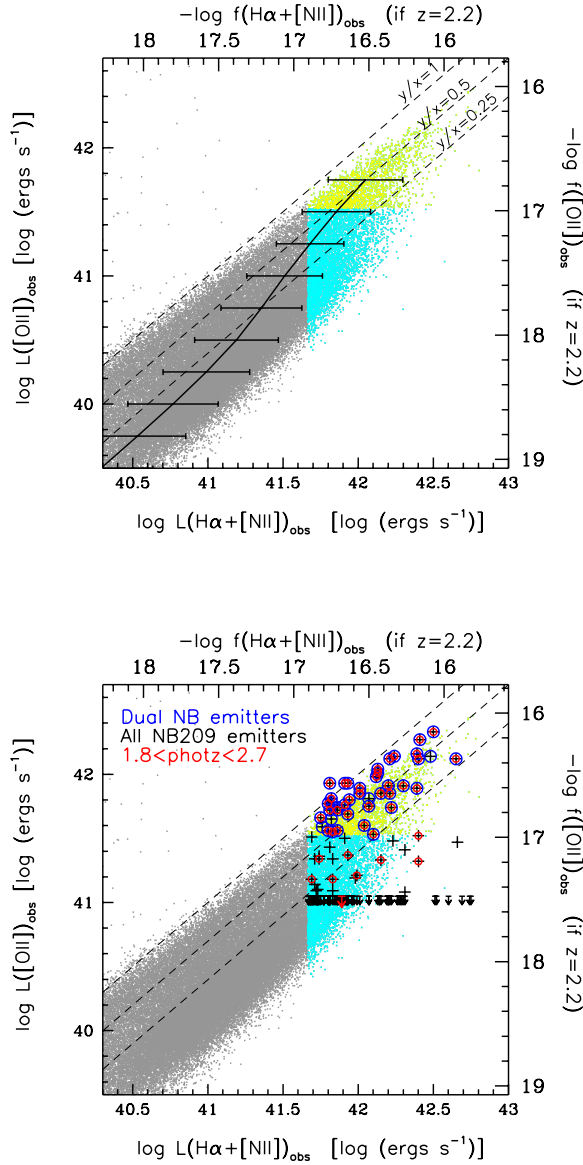


Fig. 8.— Top: $[\text{OII}]\lambda 3727$ and $\text{H}\alpha$ luminosities for local galaxies in the SDSS DR7 sample. The emission-line flux sensitivity limits of the New $\text{H}\alpha$ FourStar narrowband imaging are illustrated by showing the SDSS galaxies whose $\text{H}\alpha$ emission would be detectable in the NB210 data if they were at $z = 2.2$ (yellow and cyan regions), and those which would also have their $[\text{OII}]$ detected in the NB119 data (cyan region). Median values computed in bins of $L([\text{OII}])$ are plotted along with the 1σ widths of the distributions. Bottom: The sample of NB210 excess emitters are overplotted (black crosses), and dual NB210/NB119 excess emitters are indicated (blue open circles). Objects which have photo- z 's which would make them $\text{H}\alpha$ candidates are also marked (red open circles). The dual narrowband excess technique, as implemented here, is estimated to identify $\gtrsim 80\%$ of $z = 2.2$ $\text{H}\alpha$ emitters in the sample.

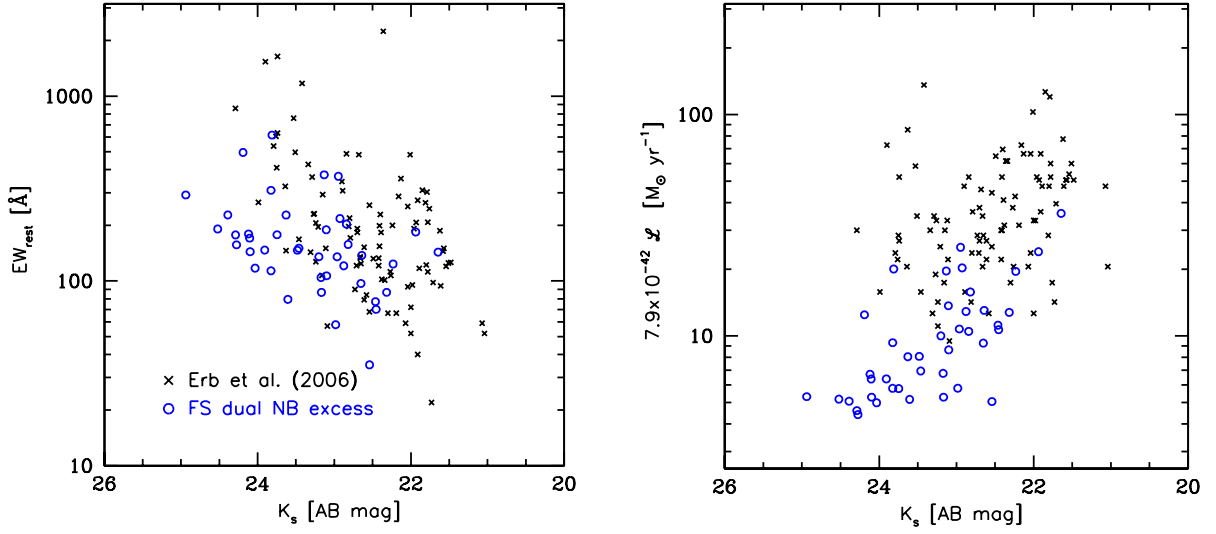


Fig. 9.— Comparison of the $z = 2.2$ dual narrowband selected $H\alpha$ emitters (blue circles) with the rest-UV selected $z \sim 2$ sample of Erb et al. (2006c) (black crosses). In both panels the plotted measurements for the $H\alpha$ emitters include both $H\alpha$ and $[\text{NII}]\lambda\lambda 6548,83$, while those for the UV-selected sample only include $H\alpha$. A factor of two correction for spectroscopic slit losses has been accounted for in the line measurements of the UV selected sample, as determined by Erb et al. (2006c). All quantities shown are as-observed, with no correction applied for dust attenuation. The left panel shows the rest-frame equivalent width, while the right panel shows the line luminosity, scaled by 7.9×10^{-42} to give indicative star formation rates (Kennicutt 1998). Both are plotted as a function of the K_s AB magnitudes. On average, narrowband $H\alpha$ sample extends the luminosities and SFRs probed for $z \sim 2$ star-forming galaxies lower by a factor of at least two.

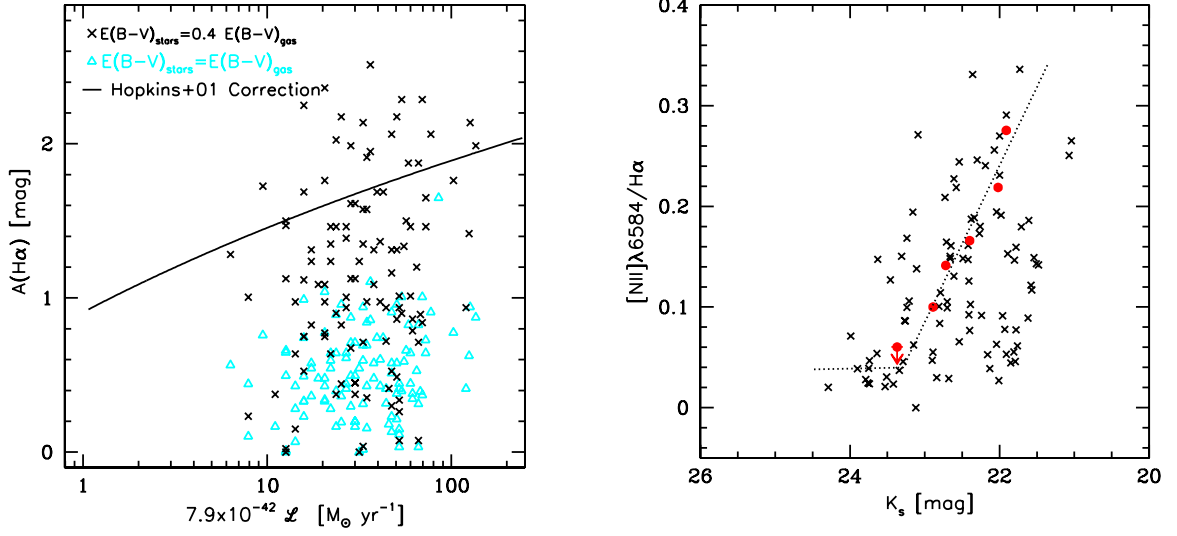


Fig. 10.— Tests of local empirical relations, which are frequently used to correct for dust reddening and the contribution of [NII], using the measurements of Erb et al. (2006a,b,c). Left: The attenuation of $H\alpha$ for the Erb UV selected sample is plotted as a function of observed SFR, and the curve shows the relation given by Hopkins et al. (2001). Erb et al. (2006b) provide $E(B-V)$'s derived by SED fitting, and these are scaled using the Calzetti et al. (2000) extinction law to give the attenuation in $H\alpha$, assuming that reddening in the gas is about twice that of the stars (black crosses) and that it is the same as that of the stars (light blue triangles). In either case, the Hopkins prescription will over-predict the attenuation. Right: $EW(H\alpha + [NII]\lambda 6583)$ is used to predict $[NII]\lambda 6584/H\alpha$ for the Erb UV selected sample using the local relation of Villar et al. (2008). The results are plotted as a function of K_s magnitude, to enable comparison with the Erb et al. (2006a) stacked spectroscopic $[NII]/H\alpha$ measurements (red circles). Here the local relation yields reasonable predictions, albeit with large scatter. To correct for the contribution of [NII] to the narrowband fluxes for the $z = 2.2$ $H\alpha$ emitters, the relation shown by the dotted line is used to estimate the $[NII]\lambda 6584/H\alpha$ ratio from the K_s magnitude.

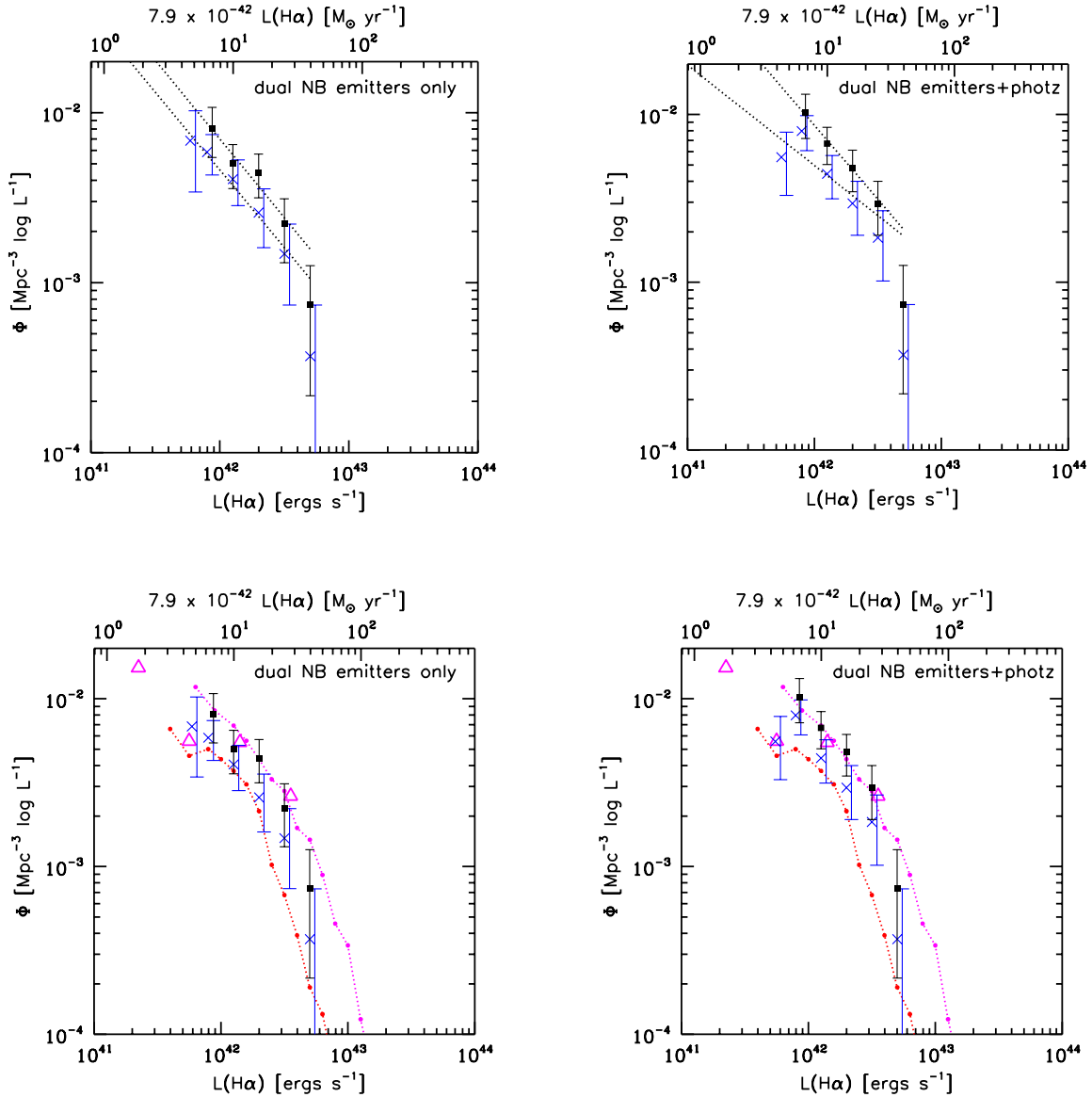


Fig. 11.— $H\alpha$ luminosity functions at $z = 2.2$. The left panels show the LFs based on the dual narrowband excess selected sample ($N=41$), while the right panels show those based on the dual narrowband excess selected sample plus NB210 excess galaxies with photo- z 's between 1.8 and 2.6 ($N=50$). In each plot, the raw observed LF (no corrections for [NII], dust, or completeness) is indicated by the blue crosses, while the LF with all of these corrections applied is given by the black squares. Error bars for the former are shown slightly offset in $L(H\alpha)$ for clarity. The top and bottom rows are identical, except that results from other recent $H\alpha$ narrowband studies are overlaid. LFs from Hayes et al. (2010) (magenta triangles), and from Sobral et al. (2012) (red curve: [NII] correction applied]; magenta curve: [NII], dust and completeness corrections all applied) are shown. Dust attenuation corrections have been made consistent with those applied here.